SCIEPublish

Article

Anisotropic Superelastic and Shape Memory Effect of Nitinol Manufactured by Electron Beam Powder Bed Fusion

Alexander Fink [1,*], Benjamin Wahlmann [1] and Carolin Körner [2]

[1] Joint Institute of Advanced Materials and Processes of Friedrich-Alexander Universität Erlangen-Nürnberg, Dr.-Mack-Straße 81, 90762 Fürth, Germany; benjamin.wahlmann@fau.de (B.W.)

[2] Chair of Materials Science and Engineering for Metals of Friedrich-Alexander Universität Erlangen-Nürnberg, Martensstraße 5, 91058 Erlangen, Germany; carolin.koerner@fau.de (C.K.)

* Corresponding author. E-mail: alexander.fink@fau.de (A.F.)

Received: 5 March 2024; Accepted: 31 March 2024; Available online: 9 April 2024

ABSTRACT: This study explores the impact of energy input and build orientation on the anisotropic mechanical and functional properties of Ti-rich Nitinol (NiTi) produced via electron beam powder bed fusion (PBF-EB), integrated with layerwise in-situ monitoring of the melted surface via backscatter electron detection (ELO). NiTi, a binary alloy of nickel and titanium, exhibits shape memory and superelasticity, making it widely used in biomedical applications and sustainable technologies. PBF-EB, particularly with ELO, is highlighted for its advantages in producing crack-free NiTi with tailored microstructures. The investigation reveals that energy input significantly influences microstructure phases, with higher energy promoting increased evaporation of Ni and enhancing Ti-rich Ti_2Ni precipitates, allowing for tailored material properties. Build orientation also proves crucial, impacting mechanical responses and functional properties. The 0° orientation yields the hardest mechanical response with the highest ultimate tensile strength (UTS) and the highest strain recovery ratio while the 45° orientation shows improved ductility but lower UTS. The influencing factors towards the formation of the anisotropic material properties are explained and the potential of tailoring the NiTi properties for specific applications by controlling energy input and build orientation in the PBF-EB process are underlined. These insights offer valuable criteria for designing innovative NiTi parts.

Keywords: Shape memory effect (SME); Superelasticity; Anisotropy; Nitinol (NiTi); Thermomechanical compression test; Electron Beam Powder Bed Fusion (PBF-EB); Electron-Optical Process Monitoring (ELO)

1. Introduction

The binary alloy Nitinol (NiTi), consisting of nickel and titanium, is the most commonly used shape memory alloy. With its exceptional functional properties of restoring its shape after mechanical deformation through a thermally induced martensite phase transition and the so-called superelasticity resulting from the stress-induced martensite phase transition. If the material exhibits either superelastic or shape memory properties depends mainly on the stable phase present at the operation temperature. If the alloy is Ti-rich (Ti-content $x_{Ti} > 50$ at.%) the NiTi exhibits the shape memory effect at room temperature since martensite is stable [1]. Otherwise, if the alloy is enriched in Ni ($x_{Ti} < 50$ at.%) the material shows superelastic properties due to the austenite present at room temperature. In the Ni-rich region of the alloy the phase transformation temperatures react much more sensitive to the change in chemical composition where a Ni loss of approx. 1 at.% can cause a drop of the transformation temperature of ca. 80 °C [1,2]. Therefore, NiTi shows a high variability of the functional properties, but an exact knowledge about the chemical composition is necessary to understand the material response under thermomechanical loading. Due to this variability, NiTi has a wide range of applications [1,3]. Due to its low modulus of elasticity and its functional properties, the biomedical sector is one of the most important areas for NiTi applications, e.g., stents or implants [4]. In addition, the material has a high potential in terms of new sustainable technologies, e.g., heating and cooling using the elastocaloric effect [5], newly designed actuators [6] or heat engines without the usage of fossil fuels [7]. The combination of NiTi and additive manufacturing (AM), especially powder bed fusion (PBF), has gained significant interest over the last years [8–12]. Conventional

https://doi.org/10.35534/amsm.2024.10004

processes such as casting can have a higher probability of impurity pick-up compared to electron beam powder bed fusion (PBF-EB), which operates under high vacuum [8]. Extensive post-processing [13] can be avoided due to near-net-shape production, and the high freedom of design enables the development of new applications [5,6]. Furthermore, PBF-EB enables a high powder bed temperature of more than 800 °C, which suppresses cracking and residual stresses, making it possible to produce crack-sensitive materials such as NiTi [9,12,14] or other crack-sensitive materials with even the possibility to tailor the microstructure by controlling the thermal conditions [15,16]. In addition, the electron beam is not only used for melting and keeping the high build temperature, it can be also used for in-situ analysis of the build using layerwise imaging via backscatter electron detection (ELO) [17]. Based on the ELO in-situ monitoring system, the formation of the melt pool and any defects (e.g., pores, uneven surface and cracks) can be detected during PBF-EB in the earliest stage [17–19] This helps reducing the number of energy-intensive build processes and avoids the need to carry out time-intensive metallographic analyses in order to find suitable parameters for new materials [17].

Crack-free NiTi with shape memory effect and superelasticity has already been successfully produced by means of PBF-EB [9,12,14,20]. The chemical composition and the related ratio of equilibrium phases (austenite (B2)/martensite (B19') NiTi, Ti_2Ni) are highly influenced by evaporation due the PBF-EB process. The phase contents, in turn, can have an enormous impact towards the mechanical and functional properties [1,2]. In this study Ti-rich NiTi is used which is not as sensitive to the change in functional properties due to changes in the chemical composition [2]. A benefit for future applications of Ti-rich NiTi is a defined transformation temperature e.g., an austenite finish temperature A_f of approx. 100 °C independently from the manufacturing. The temperature A_f displays the temperature at which all martensite transformed to austenite. However, the controllable Ni-loss via the energy input can be used as a tool to manipulate the microstructure in order to tailor the mechanical properties. A similar technique has been applied to a TiAl alloy before [21]. Additionally, the functional properties of NiTi can also be adjusted through the Ni-content [2], which could be controlled by the process parameters of PBF-EB using Ni-rich NiTi. As already shown in the manufacturing of shape memory alloys via laser powder bed fusion (PBF-LB), the build orientation influences the functional and mechanical properties [22–28]. Regarding new possible applications, the choice of the build orientation with an anisotropic material response offers an interesting new field in research.

The goal of this study is to investigate the influence of the energy input and the build orientation of PBF-EB integrated with ELO in-situ monitoring towards the anisotropic mechanical and functional properties of Ti-rich Ni-Ti. Furthermore, the aim is to get insight towards the complex interaction between the as-built PBF-NiTi texture and grain structure and the anisotropic character of as-built PBF-EB NiTi. The outcome of this study can be used to tailor the properties of a NiTi part specifically to the needs of an application.

2. Materials and Methods

2.1. Process Window Via In-Situ Electron Optical Imaging Characterization

A pre-alloyed, Ar-atomized Ti-rich binary NiTi powder with a Ti-content x_{Ti} of 51.1 ± 0.3 at.% provided by Eckart TLS GmbH (Bitterfeld-Wolfen, Germany) was used for the PBF-EB manufacturing of the samples in this work. This chemical composition was analyzed using Inductively Coupled Plasma Atomic Emission Spectroscopy (ICP-AES, Ciros CCD, Spectro Analytical Instruments GmbH, Kleve, Germany). The phase transition temperatures, Differential Scanning Calorimetry analysis (DSC, Netzsch, Selb, Germany) of the powder was performed in a temperature range from −100 °C to 150 °C with a constant heating and cooling rate of 10 K/min. The powder particles exhibited spherical morphology with a small number of satellites analyzed by SEM (SEM Quanta 450, FEI, Hillsboro, OR, USA). Based on the laser diffraction analysis (Mastersizer 3000, Malvern Panalytical GmbH, Kassel, Germany), the NiTi powder showed a particle size ranging between 45 µm and 125 µm examined. The powder shows an austentite finish temperature of A_f = 93 °C and a martensite finish temperature M_f = 24.5 °C. These values can be expected for Ti-rich NiTi with this Ti-content. A more detailed powder characterization of this powder was presented by Fink et al. [9]. To determine the processing window for NiTi PBF-EB regarding porosity and cracking tendency, specimens were fabricated on a PBF-EB machine Freemelt One (Freemelt Holding, Mölndal, Sweden) and analyzed by an electron-optical (ELO) in-situ imaging system. After melting each layer, the surface of the specimens was imaged by ELO monitoring and categorized as dense, porous, or cracked. The characterization was done via image analysis, if no black defect was detected on the molten surface the sample was defined as dense and crack free. A more detailed description of the process window generation was presented by Pobel et al. [29] and about the detection of cracks by Bäreis et al. [18]. Table 1 lists the fixed PBF-EB process parameters for the generation of the NiTi process window study. l_{cube} denotes the edge length of the produced NiTi cubes. The lateral velocity (v_{lat}) was varied as a function of the beam

velocity v_{beam} (see Equation 1), and the area energy (E_A) was adjusted as a function of the beam power P_{beam} (see Equation 2) in order to find suitable parameters for producing dense and crack-free samples. The hatch-spacing l_0 was kept constant at 200 µm. The as-built NiTi exhibits an austenite finish temperature (theoretically 100% austenite) A_f of 99 °C and a martensite finish temperature (theoretically 100% martensite) M_f of 42 °C [9].

$$v_{lat} = \frac{v_{beam} \cdot l_0}{l_{cube}} \quad (1)$$

$$E_A = \frac{P_{beam}}{v_{beam} \cdot l_0} \quad (2)$$

Table 1. PBF-EB process parameters for the ELO process window.

Process Parameter	Value
Build temperature T_{build}	~820 °C
Cube length l_{cube}	15 mm
Layer height	75 µm
Hatching	Cross-snake
Hatch distance l_0	200 µm
He—pressure	2×10^{-3} mbar
Acceleration voltage HV	60 kV

2.2. Influence of the Energy Input

A specimen (cube 15 × 15 × 15 mm^3) with a constant v_{lat} and linearly increasing area energy from 2 J/mm² to 6 J/mm² over the build height of 15 mm was built. The same cross-sectional area was used as for the samples from 2.1. The melt pool geometry was captured each layer by ELO monitoring and the maximum melt pool length was measured. The area fraction of precipitates was calculated based on binarized images from a scanning electron microscope (SEM Quanta 450, FEI, Hillsboro, OR, USA). The scanned area extends over the whole build height as shown in Figure 1 (red dashed area). The local chemical composition of the cross-sections in the as-built samples was investigated in 6 regions (blue dashed areas in Figure 1) with equal distance in between taken using electron probe microanalysis (EPMA, JXA 8100, JEOL, Tokyo, Japan). SEM analysis and EPMA were carried out after grinding, polishing, and ion milling (EM TIC 3X, Leica Microsystems, Wetzlar, Germany). The pure element standards (Ti, Ni) were used as reference for the EPMA. Images with the size of 100 × 100 µm² were taken with an interval of 50 µm as step interval, a dwell time of 200 ms, an acceleration voltage of 20 kV and a probe current of 2e^{-8} A.

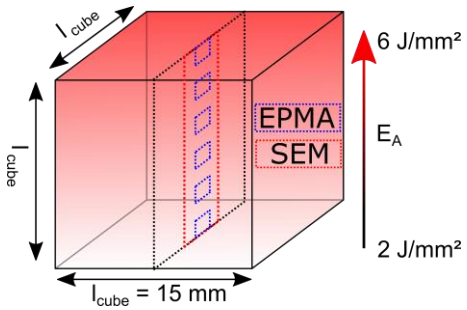

Figure 1. Sample with increasing energy input depending on the build height. The SEM analysis and EPMA measurement sites are marked.

Tensile tests were performed on samples with area energy input from 2.25 to 4.5 J/mm². The samples were built standing (0°, see Section 2.3). The tests were carried out according to DIN 50125:2016-12 [30] (Geometry B, M6) on a universal testing machine (Instron 4505 Retrofit, Instron Corporation, Canton, MA, USA) at room temperature using a strain rate of 0.018 min^{-1}. For each chosen energy input four tensile specimens were built and individually tested. The average ultimate tensile strength (UTS) and fracture elongation with a standard deviation is calculated from the experiments.

2.3. Influence of the Build Orientation

For the analysis of the influence of the build orientation on the microstructure, mechanical, and functional properties, fixed process parameters of v_{lat} = 8 mm/s and E_A = 3 J/mm² were chosen. Standing (0° deviation between build direction BD and loading direction LD), lying (90° orientation BD to LD) and diagonal specimens (45° orientation BD to LD) were built and tested. The arrangement of the testing samples on the start plate is shown in Figure 2a, and the CAD layout as well as as-built samples on the start plate are compared in Figure 2b.

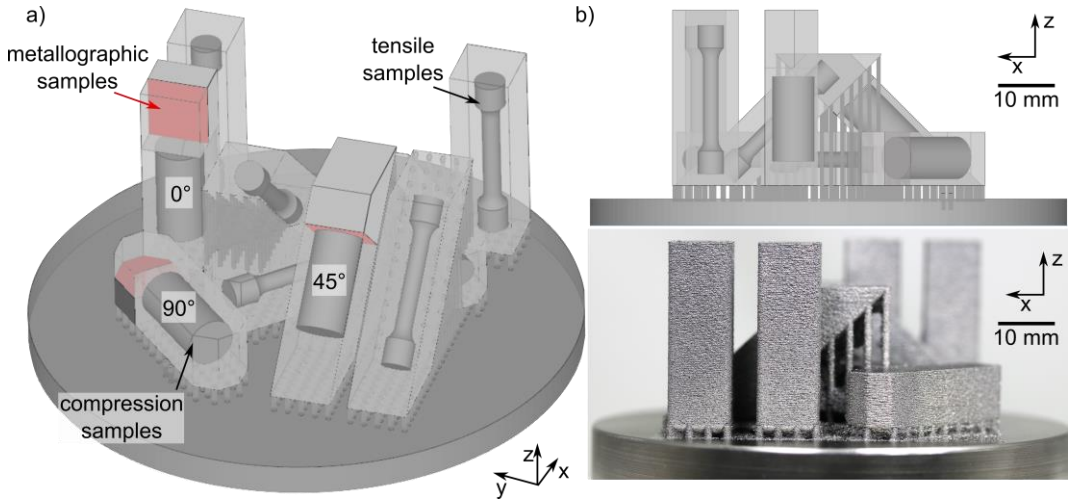

Figure 2. (**a**) Isometric view of the start plate with the planned post-processed specimens for metallographic, compression and tensile samples shown in the semi-transparent as-built parts; (**b**) Comparison between the CAD and the as-built start plate.

Microstructure characterization was carried out using an optical microscope (AXIO Imager M1m, Carl Zeiss Jena GmbH, Jena, Germany). Prior to the microstructure analysis, the PBF-EB-produced cuboid samples were cut along the BD (z) and polished with a 1 µm diamond finish. Microhardness tests (Leco M-400-G, Saint Joseph, MI, USA) were performed on 15 sites equally distributed over the height of the metallographic samples after the optical analysis. Tensile tests were performed as specified in Section 2.2.

Thermomechanical compression cycling tests (training) were carried out on a Gleeble 3500 machine (Dynamic Systems Inc., Poestenkill, NY, USA) using PBF-EB specimens to characterize the shape memory properties resulting from the thermally induced austenite/martensite phase transition. The test specimens were fabricated with the aspect ratio given in DIN 50106:2016-11 [7,31] (L = 16 mm, r = 4 mm) by wire erosion. The test procedure developed on the Gleeble machine has been explained in more detail in a previous study on determining the reversible strains caused by the phase transition and is summarized in Figure 3a [9]. During the compressive tests, the strain rate was set to 0.5 mm/min. The specimen was heated and cooled using Joule heating at a pre-stress of 25 MPa. The loading was released to the pre-stress after the desired strain for each cycle was reached. The first 10 compression cycles were performed up to a strain of 5%. For the subsequent cycles, 1.5% strain was added after each two cycles until a strain of 14% was reached. The incremental increase of the pre-strain helps to possibly identify the strain where slip starts and the irreversible strain ratio increases. The procedure of the thermo-mechanical SME cycling is demonstrated schematic for the first three cycles in Figure 3a). In addition to the shape memory cycling, the superelastic properties resulting from the stress-induced phase transition were characterized by cyclic compression tests at a constant temperature of 120 °C (~20° higher than A_f), which can be seen in Figure 3b) for the first three cycles. Again, the sample was loaded until the desired pre-strain of 2% was reached. Every cycle, this pre-strain was elevated by 1%, ending at 10% after a total of 9 cycles. After attaining the pre-strain, the sample was unloaded down to 25 MPa. To compare the shape memory effect and the superelastic effect, the recovery ratio φ_n of each cycle n was calculated using Equation 3:

$$\varphi_n = \frac{\varepsilon_{max,n} - \varepsilon_{start,n+1}}{\varepsilon_{max,n}} \quad (3)$$

The difference of the maximum strain $\varepsilon_{max,n}$ reached in cycle n and the starting strain $\varepsilon_{start,n+1}$ of the upcoming cycle n + 1 divided by $\varepsilon_{max,n}$ represents the recovery rate of each cycle. Figure 3 represents the previous explained experimental procedure on the Gleeble 3500 for the SME cycling (Figure 3a) and the SE cycling (Figure 3b). The focus in the results section is set towards the stress-strain response and the temperature axis is for the sake of simplicity not plotted.

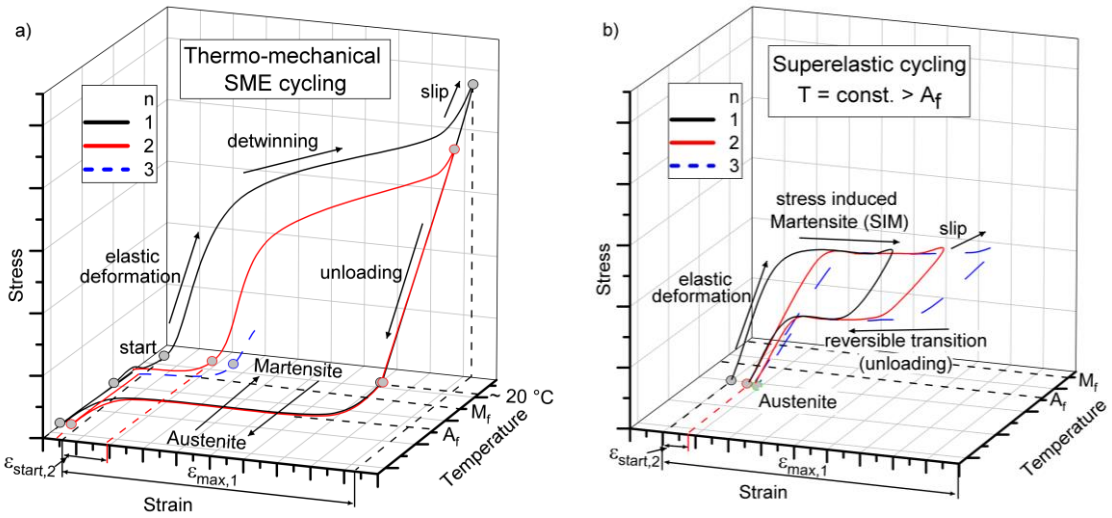

Figure 3. A schematical experimental procedure at the Gleeble 3500 for the sake of simplicity shown for the first three cycles. (**a**) The thermo-mechanical SME cycling starts with the elastic deformation of the martensite ($T < M_f$), then the material deforms via detwinning and reorientation, subsequently a thermal induced phase transition to austenite due to heating to 120 °C ($T > A_f$) follows after unloading. Adapted from [9]; (**b**) The superelastic cycling is performed at constant 120° ($T > A_f$) with a reversible stress induced martensite (SIM) transition after elastic deformation. Slip at higher strains could lead to an increase in the irreversible strain for both cycling tests.

3. Results

3.1. Process Window Via In-Situ Electron Optical Imaging Characterization

The PBF-EB process window for dense and crack-free NiTi by layerwise ELO monitoring is shown in Figure 4 with three exemplary images from surfaces representing cracked, dense, and porous samples. The area energy E_A is plotted over the lateral velocity v_{lat}.

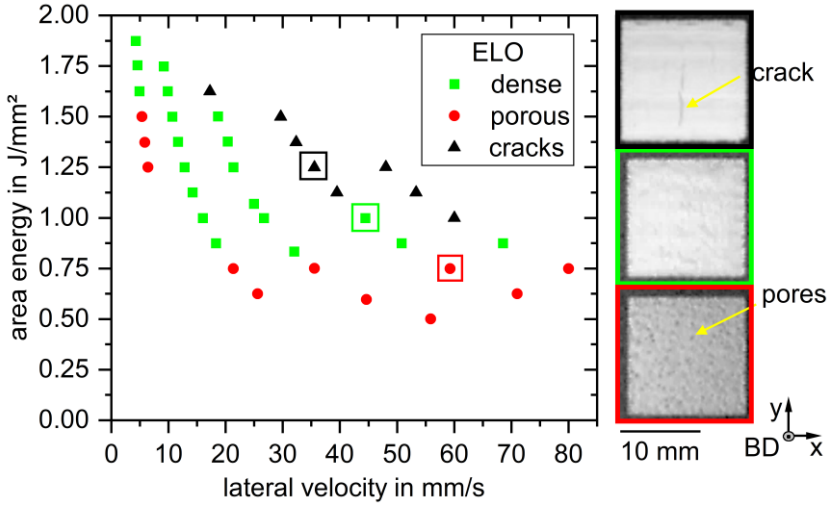

Figure 4. PBF-EB process window for dense and crack-free NiTi via in-situ electron optical imaging characterization with an exemplary porous (red), dense (green) and cracked (black) surface.

The layerwise ELO monitoring allows detecting porosity and cracks in the material in-situ. Hence, the samples can be categorized as porous, dense, and cracked during a running build job. The area energy input E_A as well as the lateral velocity v_{lat} can be adjusted simultaneously. With this method, a parameter region for dense and crack-free NiTi (green marks) was established for v_{lat} between 10–30 mm/s and E_A between 0.75 and 1.5 J/mm². For $v_{lat} \approx 10$ mm/s, the cracking tendency and porosity formation are minimal, allowing the highest variability of the area energy for achieving dense samples. The process window could be determined with just one build job and without extensive post-processing and metallographic analysis of the samples.

3.2. Influence of the Energy Input

The following section focuses on the results regarding the influence of the energy input towards tailoring the melt pool shape, chemical composition, microstructure, and mechanical properties.

3.2.1. Melt Pool Shape Characterization by In-Situ Electron-Optical Monitoring

Since the melt pool shape can be used to draw conclusion about the final microstructure [15], the lateral melt pool extension of every layer of the sample was measured. The melt pool extension and the associated ELO images are displayed in Figure 5. The colored points represent the values determined from the ELO images on the right side with the correspondingly colored frames.

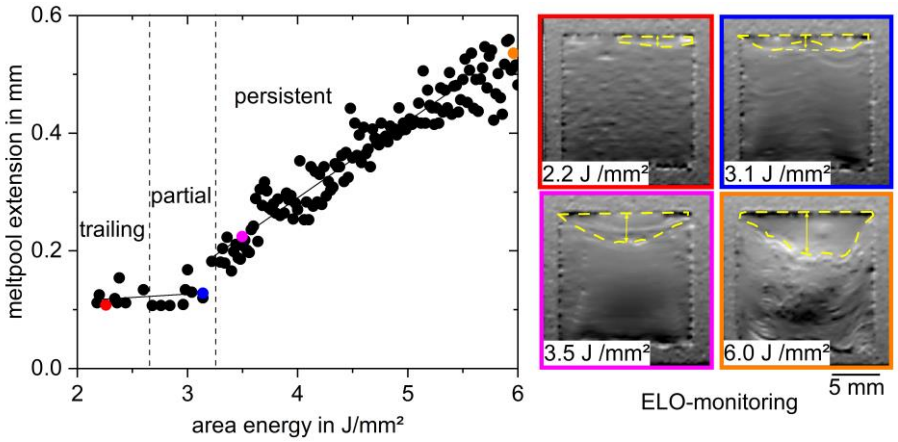

Figure 5. The melt pool extension over the area energy E_A and exemplary images from the ELO monitoring. The color of the frame from the ELO images corresponds to the highlighted points in the graph. The yellow dotted line displays the contour of the melt pool and the arrow the melt pool extension in the middle of the sample.

At E_A < 2.7 J/mm², the melt pool is trailing, and its lateral extension does not increase with higher area energy. Between 2.7 J/mm² and 3.3 J/mm², a partial-persistent melt pool evolves. Melt pools at the sample edge overlap since the local return time of the beam is shorter at the turning points than in the middle of the specimen. If E_A > 3.3 J/mm², the melt pool reaches the persistent state, and the lateral melt pool extension shows a linear increase with E_A.

3.2.2. Chemical Composition and Precipitates

The EPMA mappings (Figure 6a,b) display the local chemical composition of the microstructure at different E_A. The average of the Ni content x_{Ni} was calculated and plotted in Figure 6c depending on E_A. The colored marks correspond to the accordingly colored EPMA mappings in Figure 6a,b. Figure 6d shows the area fraction of the precipitates based on binarized SEM analysis carried out over the complete build height.

The average Ni content tends to decrease with increasing area energy due to preferential evaporation of Ni. The EPMA plots allow classifying the precipitates as Ti_2Ni due to the stoichiometric ratio of $x_{Ni} \approx 33$ at.% measured at the Ti-rich areas. In addition, the EPMA plots visualize qualitatively the increase in area fraction of the of Ti_2Ni phase with higher area energy. For the quantitative measurements, the SEM images were used since a larger area of the samples could be analyzed. The area fraction of precipitates increases linearly at E_A > 3.3 J/mm² whereas the area fraction stays constant at lower E_A. However, it is worth noting that the resolution of the SEM and EPMA is insufficient to clearly detect the absolute number of precipitates at area energies below 3.3 J/mm² since the precipitates are expected to be smaller than the resolution of the devices. No distinct precipitates are visible in Figure 6a. The image analysis tool cannot distinguish between matrix and precipitates at this resolution. CALPHAD simulations using Thermo-Calc software and the database TCTI2 were performed to evaluate the difference between the measured and the expected number of the precipitates. (see Supplemental Figure S1). For this study the focus is set on the increasing trend of the area fraction rather than on the absolute number of precipitates.

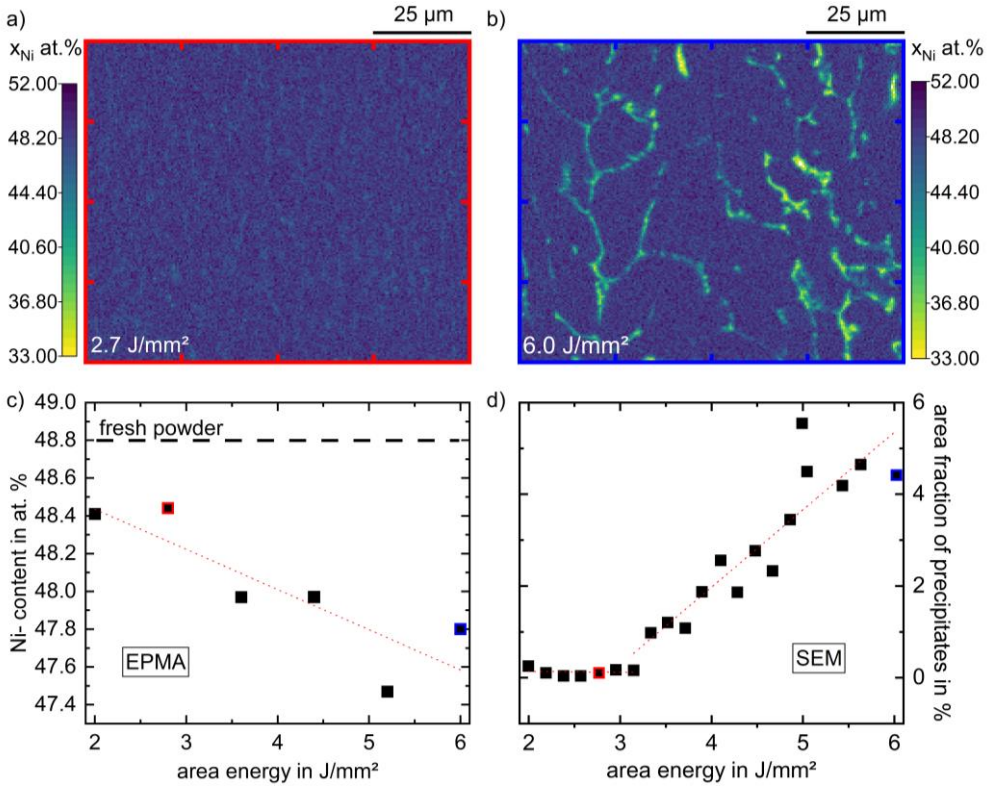

Figure 6. (**a**,**b**) Distribution of Ni content x_{Ni} at E_A = 2.7 J/mm² and E_A = 6.0 J/mm² measured via EPMA; (**c**) Average x_{Ni} determined by EPMA analysis in dependence of the area energy compared with the x_{Ni} of the fresh powder; (**d**) Area fraction of precipitates in dependence of the area energy measured via image analysis based on SEM measurements.

3.2.3. Tensile Properties

Four characteristic tensile stress-strain curves for each NiTi sample manufactured with area energies from 2.2 J/mm² to 4.5 J/mm² are plotted in Figure 7a. Figure 7b shows the UTS on the left y-axis (black) and the fracture elongation on the right y-axis (red) for all specimens measured. The lateral velocity v_{lat} was constant (8 mm/s).

The as-built Ti-rich NiTi exhibits in all samples a small detwinning and reorientation region (further only named detwinning region) starting at about 0.6–0.8% strain without a distinct stress plateau in the stress-strain curves. The highest UTS of ca. 1200 MPa could be reached for E_A = 3.75 J/mm² while the highest fracture elongation of ca. 4% was achieved using the lowest tested E_A = 2.25 J/mm². For area energies up to 3.75 J/mm², increasing E_A does not affect the UTS or fracture elongation notably with all samples exhibiting a fracture elongation > 3.5% and a UTS > 1000 MPa. After reaching E_A > 3.75, the fracture elongation (<2.6%) as well as the UTS (<900 MPa) drop, and the standard deviation of the experimental data rises significantly, indicating a more brittle mechanical behavior.

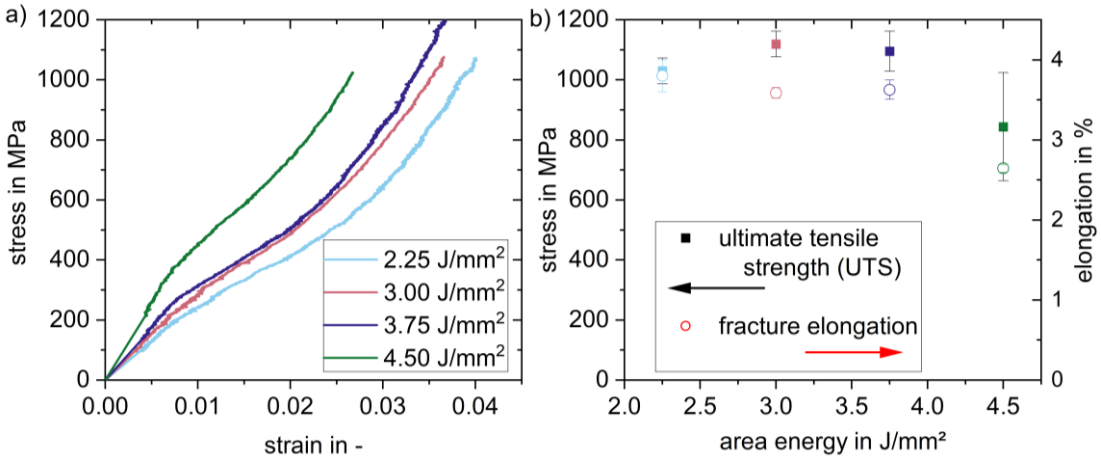

Figure 7. (**a**) Stress-strain curves for exemplary samples at room temperature (martensite) with E_A from 2.25 J/mm² to 4.50 J/mm². (**b**) Ultimate tensile strength (UTS) on the left y-axis and fracture elongation on the right y-axis for all samples tested. All samples were built standing (0°) with a constant v_{lat} = 8 mm/s.

3.3. Influence of Build Orientation

In the following chapter the outcome of the study on the influence of the build orientation towards the microstructure, mechanical und functional properties is presented. The color red represents the results for the standing 0°, blue for the diagonal 45°, and black for the lying 90° orientation.

3.3.1. Microstructure and Hardness

The as-built microstructure of PBF-EB NiTi shows a notable difference when analyzed at different angles to the build direction. In Figure 8 three different optical microscope images for samples built in different angles to the start plate are shown. The metallographic samples were cut parallel to the loading direction (see Figure 2a, red planes). In addition, the hardness values corresponding to the images are shown in Table 2.

When cutting parallel to the build direction, a columnar microstructure with lens-shaped precipitates aligned parallel to the build direction BD is observed. If cut at an angle of 45° to the BD, the area fraction of the precipitates increases due to the oblique cut. In some regions, the precipitates appear to form necklace-like structures. Cross-sections perpendicular to the BD reveal extensive necklace-like precipitate structures. Scheil calculations using CALPHAD suggest that these are Ti_2Ni phases that form in the interdendritic region. Furthermore, round pores that originate from gas trapped in the powder are visible in the 90° sample.

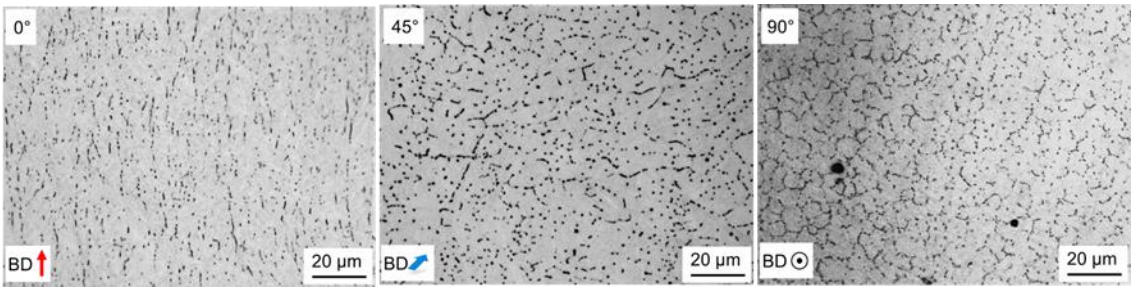

Figure 8. Microstructures of cuts in different orientations to the BD. The 0° sample shows long lens-shaped precipitates; in 90° direction the precipitates appear in a necklace-like structure. The 45° orientation is a mix of both while some precipitates seem to increase in size due to the oblique cut.

Table 2. Hardness results at different angles to the build direction.

∡ BD	HV0.2
0°	217 ± 7.70
45°	221 ± 9.26
90°	216 ± 10.56

The orientation of the test surface to the build direction shows no distinct influence on the hardness values, which lie around 218 HV0.2. The standard deviations of the measurements at different orientations (about 9 HV0.2) is higher than the hardness differences between the build orientations (1 to 5 HV0.2).

3.3.2. Tensile Properties and Failure Analysis (RT)

Tensile tests were performed to investigate the influence of the build orientation on the mechanical properties. Three stress-strain curves for the tested build orientations are shown in Figure 9a. Figure 9b depicts the corresponding fracture surfaces of the specimens.

At 0° orientation, the material exhibits the stiffest behavior characterized by the highest maximum tensile stresses > 1200 MPa and the shortest detwinning length < 2%. The fracture surface shows a transgranular brittle fracture which started in the middle of the specimen. The crack's point of origin could be a defect like a gas pore. In contrast to the 0° direction, at 45° orientation, an extended detwinning region is observed. The fracture surface exhibits an intergranular oblique brittle fracture with crack initiation starting at the machined outer surface. Finally, at 90° orientation, premature failure is evident, with stiffness levels lying between 0° and 90°. This orientation is associated with intergranular brittle fracture perpendicular to the loading direction.

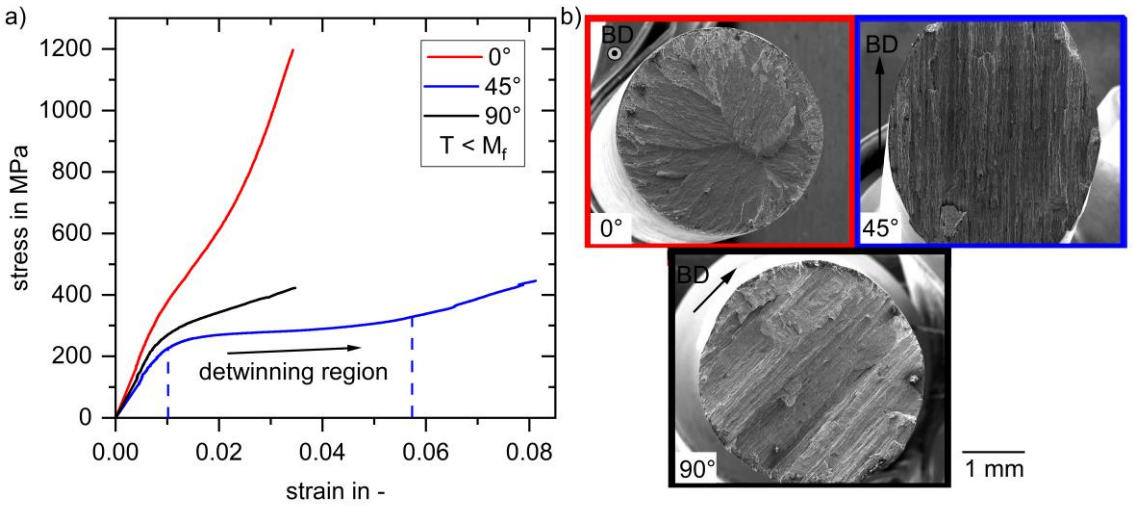

Figure 9. (**a**) Stress-strain curves at room temperature ($T < M_f$) for the tested build orientations (0°, 45°, 90°). The process parameters were kept constant (v_{lat} = 8 mm/s and E_A = 3 J/mm²); (**b**) Corresponding fracture surfaces of exemplary specimens for each build direction.

3.3.3. Superelastic Compression Properties (120 °C)

The stress-strain curves obtained from the superelastic compression cycling experiments are displayed in Figure 10a–c for the three tested build directions. Figure 10d compares the recovery rate in dependence of the pre-strain for each cycle.

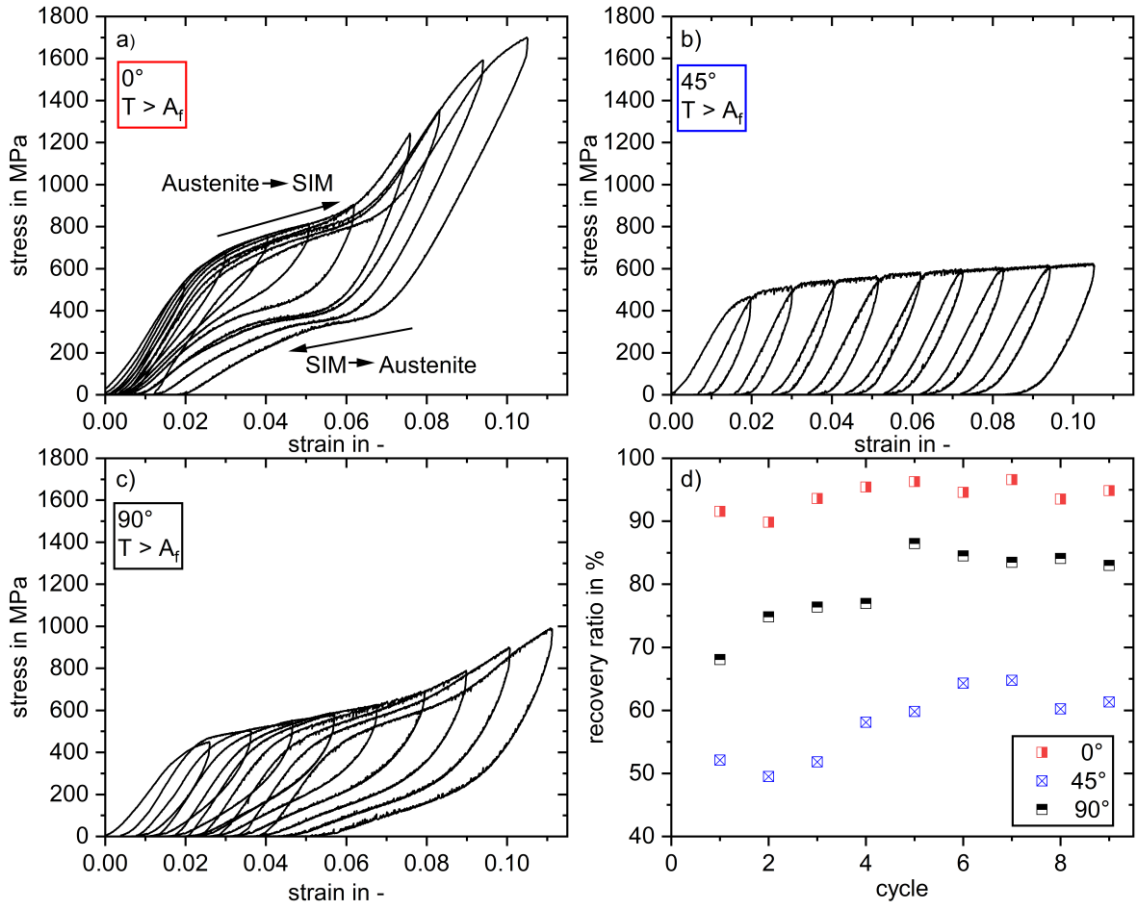

Figure 10. Superelastic compression cycling at T = 120°C (>A_f) for (**a**) 0° build orientation; (**b**) for 45° build orientation and (**c**) for 90° build orientation; (**d**) Comparison of the recovery ratio due to superelasticity for all tested build orientations over the cycles. The process parameters were kept constant (v_{lat} = 8 mm/s and E_A = 3 J/mm²). The stress induced martensite (SIM) transformation is marked exemplary in the (**a**).

At 0° orientation, the material exhibits a superelastic plateau due to the stress induced phase transition from austenite into martensite that initiates at approximately 600 MPa and 2% strain, followed by a steady increase of the slope after reaching a strain of 6%. After unloading, a distinct stress-strain superelastic hysteresis occurs with an unloading plateau stress of ca. 300 MPa for all cycles. For 90° samples, the plateau starts at 450 MPa and 2% strain. The rising slope begins at a strain of 7.5%. After unloading, a hysteresis without a distinct plateau is measured. Furthermore, the maximum compression stress after applying 10% strain is significantly lower for 90° (990 MPa) compared with 0° (1750 MPa). At 45° orientation, the plateau begins at approximately 450 MPa at 2% strain and the hysteresis is barely observable. Even after 10% strain a maximum compression stress of only 600 MPa is achieved. The differences become readily apparent upon comparing the recovery rate in Figure 10d. While the sample built standing (0°) reaches a recovery rate of > 90%, the 45° exhibits maximum 62%, the 90° sample lies in between. All samples have a trend to higher recovery after 4 cycles after a pre-strain of 5%.

3.3.4. Shape Memory Properties (Thermomechanical Compression Cycling)

The build orientation also has an impact on the shape memory properties, which can be seen in Figure 11. The SME stress-strain cycling curves up to a pre-strain of 14% are depicted in Figure 11a–c while the recovery rate for the first 9 training cycles is plotted in Figure 11d.

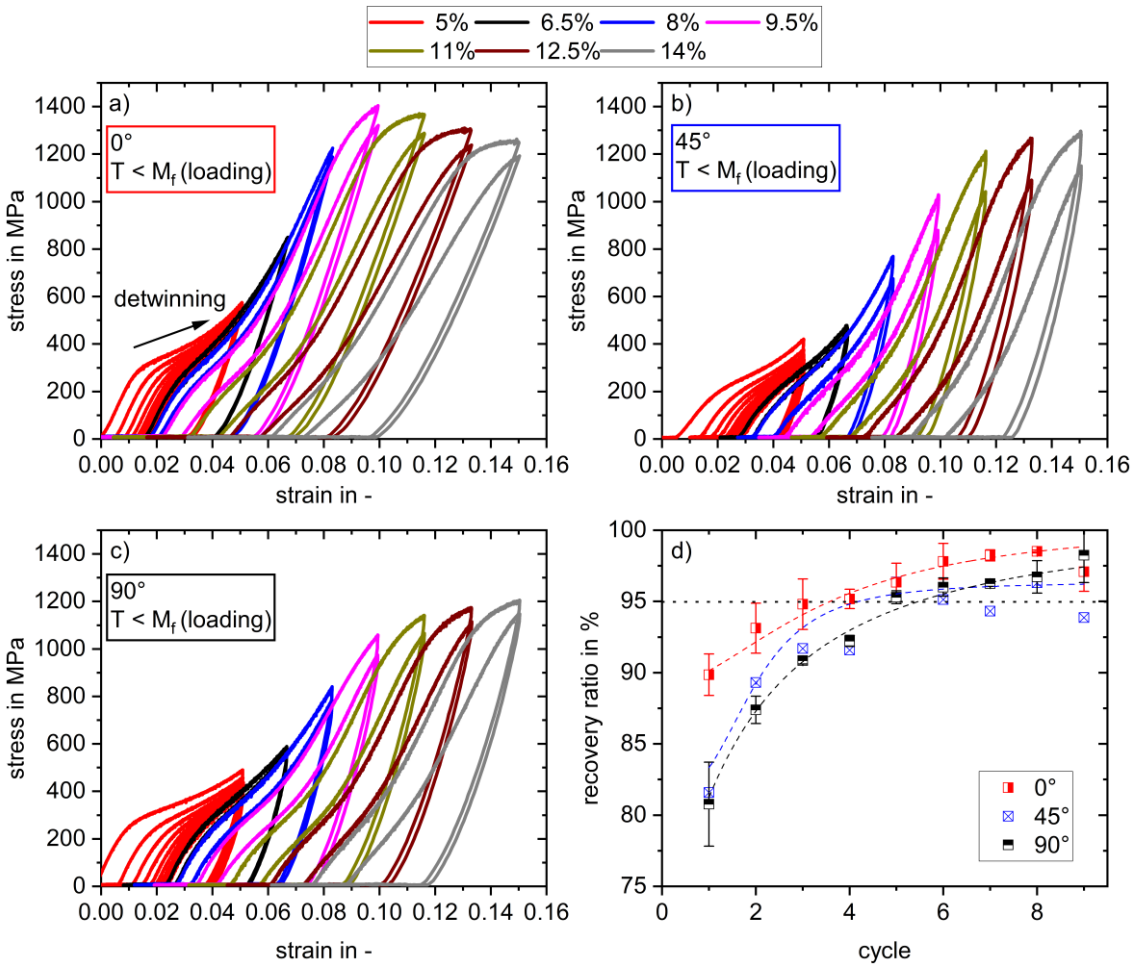

Figure 11. SME stress-strain cycling for (**a**) 0° build orientation; (**b**) 45° build orientation and (**c**) 90° build orientation; (**d**) Comparison of the recovery ratio due to the SME training in all tested build orientations over the training cycles 1–9 with 5% pre-strain. The process parameters were kept constant (v_{lat} = 8 mm/s and E_A = 3 J/mm²). The loading was performed at room temperature ($T < M_f$).

The material demonstrates its stiffest behavior in 0° direction, characterized by the highest maximum compression stresses and the shortest detwinning region. The stress at which the detwinning and reorientation of the martensite starts shows a similar trend as the tensile tests: the lowest is achieved at 45° and the highest at 90°. Regarding the maximum compression stresses of each cycle, the 45° and 90° samples show a similar response up to a strain of 8%. At strains > 8%, the 90° orientation sample shows a decreasing slope of the stress-strain curve after 1000 MPa and does not reach values > 1200 MPa. The slope of the 45° sample stays constant up to ca. 1150 MPa and surpasses the maximum

compression stresses reached at 90°. However, the differences between the build orientations are not as significant as for the superelasticity or tensile tests. Comparing the recovery rates of the first 9 training cycles across all samples, it becomes apparent that the 90° and 45° samples exhibit less recovery compared to the 0° sample. This trend is even more pronounced in the first 5 cycles. As a consequence, for the as-built NiTi training of the 0° direction, the highest stress (580 MPa) was needed to reach the highest recovery rates (max. 99%), while the 45° sample was only loaded up to 415 MPa and reached the lowest recovery (max. 95%).

4. Discussion

4.1. Efficient and Sustainable PBF-EB NiTi Process Window Generation by ELO

In previous studies it was shown that layerwise ELO monitoring can detect porosity [17] as well as the cracking tendency [18]. These two methods were applied to generate a process window for manufacturing dense and crack-free NiTi via PBF-EB. The results for the porosity are in good agreement with previous studies for Ti-rich NiTi [9] and equiatomic NiTi [14] via PBF-EB. Due to the high number of brittle precipitates in Ti-rich NiTi, this study focuses on the cracking tendency. The precipitation combined with the high thermal gradients and the high cooling rates characteristic for PBF-EB can lead to a high cracking susceptibility [32]. A higher v_{lat} leads to a higher cooling rate and a higher E_A leads to a higher thermal gradient as well as an elevated evaporation of Ni. All of these effects lead to a higher crack tendency at high E_A and a narrowing of the process window at high v_{lat}. which can be seen in Figure 4. This narrowing is seen especially at v_{lat} > 30 mm/s. The increasing cracking tendency for elevated E_A and v_{lat} was also found for the selective laser melting process (SLM) [10,32].

Furthermore, it is worth mentioning that the outcomes for the process window were conducted during only one process with alternating process parameters and without any post-processing of the samples. Consequently, with the layerwise ELO monitoring the extensive metallographic sample preparation and costly PBF-EB processes in terms of energy as well as NiTi powder acquisition can be reduced significantly. The layerwise ELO imaging provides a more sustainable and cost-efficient way to find suitable parameters for dense and crack-free materials as shown in this study for Ti-rich NiTi.

4.2. Tailoring of the Mechanical Properties by Adapting the Energy Input

The trailing-to-persistent transition for NiTi was found to be between E_A = 2.5–3.5 J/mm² for v_{lat} = 8 mm/s. After reaching the persistent state, the lateral extension increases linearly with increasing area energy. Simulations and experiments for PBF-EB presented such melt pool characteristics with increasing E_A for the nickel-based superalloy CMSX-4 [15,33] One could expect such an outcome due to the similar thermal properties of these two materials [34,35]. The control of the melt pool creates insights in tailoring of the microstructure regarding the grain size and precipitates. Other studies showed that even single crystals were accomplished by using a persistent melt pool [15]. In this study, the focus was set to the precipitation of Ti_2Ni and the evaporation of Ni as a tailoring tool for microstructure and mechanical properties.

It is known from literature on powder bed fusion that Ni evaporates from the melt pool due to the high surface temperature [12], which increases with higher energy input [25,28]. Tan et al [36] recorded a decrease of 1 at.% Ni in Ti-rich NiTi using a max. area energy of 8.4 J/mm² for PBF-LB, while in this study an evaporation of ~ 1.3 at.% Ni was present for $E_A \approx 5$ J/mm². The Ni loss could be enhanced by a persistent melt pool. In this case, high E_A causes a greater lateral extension of the melt pool and, thus, creates a larger surface area from which Ni can evaporate. Furthermore, a higher energy input also leads to elevated peak temperatures, which further intensifies evaporation. This leads to the assumption that the Ni loss can significantly increase when a persistent melt pool is present compared to a trailing melt pool. Therefore, the Ni loss leads to a shift to a higher Ti/Ni ratio and the Ti_2Ni precipitation is favored. Equilibrium CALPHAD calculations predict an increase in the fraction of precipitates by 4.8 mol.% for the measured Ni loss of ~1.3 at.%. The EPMA measurements of the Ni content and the area fraction of precipitates fit well with the theoretically calculated equilibrium data. Controlling the Ni content of NiTi by the energy input could also be applied for tailoring the transformation temperatures and thereby the functional properties [11,28]. For Ti-rich NiTi powder, no shift of the transformation temperatures is to be expected. Therefore, this study focused on the tailoring of mechanical properties exclusively through adjustment of the Ni content.

Due to the increase of the precipitates in number and size, a trend towards more brittle mechanical properties was found up to $E_A \approx 4$ J/mm². As explained in section 3.1, a higher energy input induces a higher cracking tendency. Since the process window suggests a higher cracking tendency at higher area energies, it can be concluded that at E_A > 4.5

J/mm², which lies outside the evaluated parameter range for process window determination, cracks could start to form in the material and decrease the ductility, as evidenced by the reduced fracture elongation.

By controlling the Ni evaporation, the mechanical properties (stiffness, ductility, strength) are tailorable. With an even lower Ni content of the powder, the functional properties could also be controlled by adjusting the phase transformation temperatures.

4.3. Dependency of the Functional and Mechanical Properties on the Build Direction

The microstructure of as-built NiTi shows interdendritic Ti_2Ni lens-shaped precipitates oriented parallel to the BD. In addition, previous studies found a columnar grain structure for PBF-EB NiTi [9,12,14]. The columnar grain morphology results from the thermal gradient being highest in the vertical direction. This microstructure is typical for NiTi fabricated via PBF-EB [9,36]. In the B2 phase, a $<001>_{B2}$ texture is expected in BD. Such a texture has already been measured for PBF-LB [26,27] and PBF-EB [12]. This 0° orientation shows the highest plateau stress $\sigma_{plateau}$ for the mechanical tensile tests at room temperature and SE as well SME compression tests. If analyzed perpendicular to the BD (90°), the columnar grain structure appears equiaxed and the precipitates stretch out in a necklace-like interdendritic structure. For a 90° build orientation, no clear texture was measured for PBF- laser beam (LB). [26,27]. Accordingly, mechanical and functional property values between the extremes of the 0° and 45° orientations were found in this study for the 90° sample. However, premature failure under tension was observed. The oblique cut of the grain structure at 45° leads to an apparent increase of the size of the precipitates and a necklace-like structure. In the literature, the texture for this direction was characterized as $<011>_{B2}$ [27]. The lowest plateau stresses $\sigma_{plateau}$ were measured in this direction. On the one hand, almost no superelastic stress-strain hysteresis occurred. On the other hand, the most ductile response with a fracture elongation ca. three times higher than for the 0° specimen was reached in tensile direction. Overall, the differences between the build orientation are more pronounced in tensile direction than under compression. These anisotropic outcomes for the mechanical und functional properties can be explained by a combination of several influencing factors.

First, the texture affects the mechanical properties. A model for predicting the mechanical properties of superelastic materials based on a modified Taylor factor *M*' was presented by Ono et al [37]. The conventional Taylor factor *M* relates the flow stress to the critical shear stress in polycrystalline materials. It depends on the crystallographic structure and the texture [38]. The Taylor factor allows predicting the influence of texture towards the mechanical behavior. The modification of this factor was established for the SIM transition in polycrystalline NiTi to analyze the superelastic stress-strain response to account additionally for the effects of the volume change and hydrostatic stress induced by this phase transition [37]. The modified Taylor factors *M*' for the different orientations are summarized in Table 3. The plateau stress $\sigma_{plateau}$ can be calculated using the product of *M*' and the shear stress τ (see Equation 4) while the detwinning length ε_{length} is the quotient out of a factor for martensite reorientation γ (0.13) and *M*' (see Equation 5) [39].

$$\sigma_{plateau} = \tau \times M' \quad (4)$$

$$\varepsilon_{length} = \gamma / M' \quad (5)$$

Table 3. Taylor factor M' for the three crystal orientations <001>, <011>, <111> in the B2 structure of NiTi [37].

Loading Direction	Taylor factor $M'_{tensile}$ [37]	Taylor Factor $M'_{compression}$ [37]
<001>	4.9	2.7
<011>	3.2	2.6
<111>	2.4	4.1

The model predicts that the $<001>_{B2}$ should have a higher plateau stress with less detwinning strain under tension compared to the $<011>_{B2}$ or the $<111>_{B2}$ texture due to the highest M'. In contrast, the $<111>_{B2}$ texture shows the highest *M*' under compression. The asymmetry between tensile and compression is due the fact that martensite variants [1,40,41] can only shear in one direction [37,41,42]. Laplanche et al. [39] validated this modified Taylor-based model for the reorientation and detwinning of the martensite variants. The model showed that the dependency between the orientation and SIM can also explain the mechanical response of textured martensite. Based on this theory, the $<001>_{B2}$ texture should result in higher plateau stresses with a lower detwinning as well as SIM region compared to $<011>_{B2}$. As already mentioned, the influence of the texture on the mechanical response should be more significant under tensile than under compression loading. This theoretical model explains well the difference in plateau stress $\sigma_{plateau}$ and length ε_{length} which is observable in the tensile tests for the different build orientation. The model predicts at circa an increase of 1.5 of the

detwinning stress $\sigma_{plateau}$ and detwinning region ε_{length} comparing the $<001>_{B2}$ and $<011>_{B2}$ directions. The observed difference of $\sigma_{plateau}$ between 0° and 45° fits well with the model, but the detwinning region, which is circa three times longer for the 45° orientation, cannot be explained by only using the Laplanche model. In addition, the predicted tension-compression asymmetry [37,39,42] is observed since the differences between the orientations are less pronounced when tested under the compression loading state.

The second influencing factor represents the columnar grain structure resulting from the PBF-EB process. The grains and the lense-shaped precipitates of the 45° sample are aligned in the direction of the maximum shear plane (see Figure 12). If arranged in this direction, the grain boundaries represent weak sites for crack growth, reduce the detwinning stress [43] and improve dislocation sliding in this direction [44]. In the other two directions the grain boundaries and the precipitates could act as an obstacle for dislocations, detwinning and crack propagation resulting in a strengthening of the material [26]. This influence of the grain structure can be observed in the fracture behavior, where the 45° sample showed an oblique intergranular fracture while the others fractured perpendicular to the loading direction in a transgranular manner. In addition, the strengthening due to precipitates and grain boundaries explain the higher UTS of the 0° sample.

It is important to note that cracks occurred on the fracture surface of the 90° sample. This could be due to a third factor, the residual stresses σ_{res} from the manufacturing. Those could lead to the premature failure seen under tensile loading as well as a smaller recovery ratio under compression since defects could lead to slip which degrades the reversible strain [1]. The large contact area with the start plate constrains the contraction after melting. The highest stresses occur in the longitudinal direction of the part and increase with length which could lead to cracking [45,46]. A higher build temperature or other innovative hatching strategies could reduce the residual stresses.

The fourth factor is the probability of slip in B2 austenite calculated by the Schmid-factor. The maximum Schmid factor (0.5) under compression in the B2 austenite is in the <100> {110} system [47]. A previous study showed that PBF-LB samples built in 45° direction showed the highest probability of slip with the lowest irrecoverable strain under this loading conditions [25]. The effect of diminishing superelasticity due to preferred slip is well known in solution annealed NiTi [40]. This effect can explain the low recovery ratio from the superelastic hysteresis in 45° orientation.

To summarize the discussion of the anisotropic NiTi behavior resulting from the PBF-EB process, the influencing factors are visualized in Figure 12 for the three build directions.

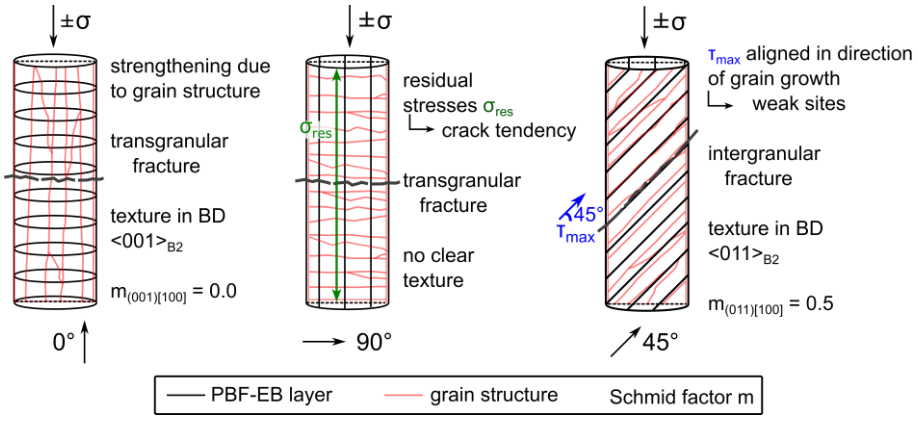

Figure 12. Summary of the influencing factors towards the three different loading and building directions, respectively. The mechanical and functional properties are based on different influencing factors, namely the texture with the resulting Schmid-factor m, the residual stresses and the columnar grain structure with the hardening effect. Data for visualization based on results of this study and literature research on PBF NiTi [12,25,27,37,44,45].

In summary, the anisotropic mechanical, SE and SME response of PBF-EB as built-NiTi is explained by a complex combination of influencing factors, namely the texture, residual stresses and grain structure. If loaded in the build direction (0°) the strongest mechanical behavior with the highest UTS and the lowest fracture elongation was achieved. Furthermore, the best strain recovery ratio (<95%) was reached for SE and SME. In contrast, the 45° orientation showed three times higher fracture elongation with a third of the UTS of the vertical samples and only 50% recovery rate under SE compression. The 90° sample showed mechanical and functional properties lying in-between the other orientations with a premature failure. A combination of the above-mentioned influencing factors must be accounted to predict the anisotropic mechanical and functional properties of PBF-EB as-built NiTi. However, with controlling the built orientation, the properties of NiTi can be tailored to the needs of the part.

5. Conclusions

The study investigates the influence of the energy input and the build orientation of PBF-EB integrated with ELO in-situ monitoring towards the anisotropic mechanical and functional properties of Ti-rich Ni-Ti. The layerwise ELO monitoring can be used to determine suitable processing parameters for fabricating dense and crack-free components in a more time- and cost-efficient and sustainable way than by metallographic sample analysis. The process parameters to gain dense and crack-free PBF-EB NiTi were in good agreement with previous published literature. In addition, it was found that the energy input impacts the phases of the microstructure significantly and can be controlled due to the high energy density of the electron beam. With rising energy input, the melt pool enlarges in the lateral direction, more Ni can evaporate, and, as a consequence, the area fraction of the Ti-rich Ti_2Ni precipitates increases. This can be used to adjust the as-built material since the amount of Ti_2Ni has a significant impact towards the mechanical properties. Furthermore, the build orientation exhibits a major influence on the microstructure and the resulting functional as well as the mechanical properties in the as-built state. Loading in the build orientation showed the strongest mechanical response with the highest UTS and the lowest fracture elongation. However, the best strain recovery ratio was achieved. In contrast, the 45° orientation showed three times higher fracture elongation with a third of the UTS of the vertical samples. This mechanical and functional behavior is explained by a combination of the texture, residual stresses, and the grain structure. It explains the complexity of the anisotropic PBF-EB as built-NiTi in terms of mechanical behavior as well as superelasticity and shape memory effect. Future research could focus on the functional and structural fatigue depending on the process parameters and the built orientation and innovative applications. A possible practical application could be a cellular PBF-EB-NiTi structure. Using the anisotropic functional properties, the structure could be designed with different stiffness and Poisson's ratio depending on the energy input and the build direction. Struts aligned parallel to the build direction could benefit from the stiffer mechanical response, while struts perpendicular or oblique to the build direction would exhibit more ductile behavior. This could be used, for example, as a cellular damping application with different stiffness depending on the load direction. However, this study demonstrated the potential to adjust the anisotropic mechanical and the functional properties by PBF-EB by controlling the process parameters.

Supplementary Materials

The following supporting information can be found at: https://www.sciepublish.com/article/pii/166, Figure S1. CALPHAD calculations of the Ti_2Ni mole fraction over the Ti-content in a binary alloy NiTi using Thermo-Calc software and the database TCTI2.

Acknowledgments

We would like to thank Sabine Michel, Kerstin Zinn and Annemone Alleborn for carrying out the sample preparation and characterizing the microstructure using SEM. We would also like to thank Michael Florian and Franz Pislcajt for post-processing the samples. Furthermore, we thank Stefan Brehm for his insightful observations in his master thesis. Finally, we would like to thank the “Chair of Reaction Engineering and Catalysis at the TU Dortmund University” for the fruitful collaboration with the project partners Dominik Rudolf and Prof. Hannsjörg Freund.

Author Contributions

Conceptualization, A.F. and C.K.; Methodology, A.F.; Formal Analysis, A.F. and B.W. and C.K.; Investigation, A.F.; Resources, C.K.; Data Curation, A.F.; Writing—Original Draft Preparation, A.F.; Writing—Review & Editing, B.W. and C.K.; Visualization, A.F.; Supervision, B.W. and C.K.; Project Administration, A.F.; Funding Acquisition, C.K.

Ethics Statement

Not applicable.

Informed Consent Statement

Not applicable.

Funding

Financial support from the German Research Foundation (DFG, Deutsche Forschungsgemeinschaft, Bonn, Germany; project number: 432515505) is gratefully acknowledged.

Declaration of Competing Interest

We declare that we have no financial and personal relationships with other people or organizations that can inappropriately influence our work, and there is no professional or other personal interest of any nature or kind in any product, service, and/or company that could be construed as influencing the position presented in, or the review of the manuscript entitled "Anisotropic superelastic und shape memory effect of Nitinol manufactured by electron beam powder bed fusion".

References

1. Lagoudas DC. *Shape Memory Alloys: Modeling and Engineering Applications*; Springer: Boston, MA, USA, 2008.
2. Farber E, Zhu J-N, Popovich A, Popovich V. A review of NiTi shape memory alloy as a smart material produced by additive manufacturing. *Mater. Today Proc.* **2020**, *30*, 761–767.
3. Van Humbeeck J. Shape Memory Alloys: A Material and a Technology. *Adv. Eng. Mater.* **2001**, *2001*, 837–850.
4. Alipour S, Taromian F, Ghomi ER, Zare M, Singh S, Ramakrishna S. Nitinol: From historical milestones to functional properties and biomedical applications, Proceedings of the Institution of Mechanical Engineers. Part H. *J. Eng. Med.* **2022**, *236*, 1595–1612.
5. Hou H, Simsek E, Stasak D, Hasan NA, Qian S, Ott R, et al. Elastocaloric cooling of additive manufactured shape memory alloys with large latent heat. *Phys. D: Appl. Phys.* **2017**, *50*, 404001.
6. Seigner J, Bezsmertna O, Fähler S, Tshikwand GK, Wendler F, Kohl M. Origami-Inspired Shape Memory Folding Microactuator. *Appl. Mech. Mater.* **2020**, *64*, 6.
7. Abubakar RA, Wang F, Wang L. A review on Nitinol shape memory alloy heat engines. *Smart Mater. Struct.* **2021**, *30*, 13001.
8. Elahinia M, Shayesteh Moghaddam N, Taheri Andani M, Amerinatanzi A, Bimber BA, Hamilton RF. Fabrication of NiTi through additive manufacturing: A review. *Prog. Mater. Sci.* **2016**, *83*, 630–663.
9. Fink A, Fu Z, Körner C. Functional properties and shape memory effect of Nitinol manufactured via electron beam powder bed fusion. *Materialia* **2023**, *30*, 101823.
10. Monu MC, Ekoi EJ, Hughes C, Kumar SS, Brabazon D. Resultant physical properties of as-built nitinol processed at specific volumetric energy densities and correlation with in-situ melt pool temperatures. *J. Mater. Res. Technol.* **2022**, *21*, 2757–2777.
11. Wang X, Yu J, Liu J, Chen L, Yang Q, Wei H, et al. Effect of process parameters on the phase transformation behavior and tensile properties of NiTi shape memory alloys fabricated by selective laser melting. *Addit. Manuf.* **2020**, *36*, 101545.
12. Zhou Q, Hayat MD, Chen G, Cai S, Qu X, Tang H, et al. Selective electron beam melting of NiTi: Microstructure, phase transformation and mechanical properties. *Mater. Sci. Eng.* **2019**, *744*, 290–298.
13. Hassan MR, Mehrpouya M, Dawood S. Review of the Machining Difficulties of Nickel-Titanium Based Shape Memory Alloys. *Appl. Mech. Mater.* **2014**, *564*, 533–537.
14. Lin Z, Surreddi KB, Hulme C, Dadbakhsh S, Rashid A. Influence of Electron Beam Powder Bed Fusion Process Parameters on Transformation Temperatures and Pseudoelasticity of Shape Memory Nickel Titanium. *Adv. Eng. Mater.* **2023**, *25*, 2201818.
15. Pistor J, Breuning C, Körner C. A Single Crystal Process Window for Electron Beam Powder Bed Fusion Additive Manufacturing of a CMSX-4 Type Ni-Based Superalloy. *Materials* **2021**, *14*, 3785.
16. Ramsperger M, Singer RF, Körner C. Microstructure of the Nickel-Base Superalloy CMSX-4 Fabricated by Selective Electron Beam Melting. *Metall. Mater. Trans. A* **2016**, *47*, 1469–1480.
17. Arnold C, Pobel C, Osmanlic F, Körner C. Layerwise monitoring of electron beam melting via backscatter electron detection. *RPJ* **2018**, *24*, 1401–1406.
18. Bäreis J, Semjatov N, Renner J, Ye J, Zongwen F, Körner C. Electron-optical in-situ crack monitoring during electron beam powder bed fusion of the Ni-Base superalloy CMSX-4. *Prog. Addit. Manuf.* **2023**, *8*, 801–806.
19. Renner J, Grund J, Markl M, Körner C. A Ray Tracing Model for Electron Optical Imaging in Electron Beam Powder Bed Fusion. *JMMP* **2023**, *7*, 87.
20. Krooß P, Lauhoff C, Gustmann T, Gemming T, Sobrero C, Ewald F, et al. Additive Manufacturing of Binary Ni–Ti Shape Memory Alloys Using Electron Beam Powder Bed Fusion: Functional Reversibility Through Minor Alloy Modification and Carbide Formation. *Shap. Mem. Superelasticity* **2022**, *8*, 452–462.
21. Knörlein J, Franke MM, Schloffer M, Körner C. In-situ aluminum control for titanium aluminide via electron beam powder bed fusion to realize a dual microstructure. *Addit. Manuf.* **2022**, *59*, 103132.
22. Dadbakhsh S, Vrancken B, Kruth J-P, Luyten J, van Humbeeck J. Texture and anisotropy in selective laser melting of NiTi alloy. *Mater. Sci. Eng.* **2016**, *650*, 225–232.
23. Ferretto I, Kim D, Lee WJ, Hosseini E, Della Ventura NM, Sharma A, et al. Shape memory and mechanical properties of a Fe-Mn-Si-based shape memory alloy: Effect of crystallographic texture generated during additive manufacturing. *Mater. Des.* **2023**, *229*, 111928.

24. Niendorf T, Brenne F, Krooß P, Vollmer M, Günther J, Schwarze D, et al. Microstructural Evolution and Functional Properties of Fe-Mn-Al-Ni Shape Memory Alloy Processed by Selective Laser Melting. *Metall. Mater. Trans. A* **2016**, *47*, 2569–2573.
25. Saedi S, Shayesteh Moghaddam N, Amerinatanzi A, Elahinia M, Karaca HE. On the effects of selective laser melting process parameters on microstructure and thermomechanical response of Ni-rich NiTi. *Acta Mater.* **2018**, *144*, 552–560.
26. Safaei K, Nematollahi M, Bayati P, Kordizadeh F, Andani MT, Abedi H, et al. On the crystallographic texture and torsional behavior of NiTi shape memory alloy processed by laser powder bed fusion: Effect of build orientation. *Addit. Manuf.* **2022**, *59*, 103184.
27. Shi G, Li L, Yu Z, Sha P, Cao Q, Xu Z, et al. Effect of crystallographic anisotropy on phase transformation and tribological properties of Ni-rich NiTi shape memory alloy fabricated by LPBF. *Opt. Laser Technol.* **2023**, *157*, 108731.
28. Wei S, Zhang J, Zhang L, Zhang Y, Song B, Wang X, et al. Laser powder bed fusion additive manufacturing of NiTi shape memory alloys: A review. *Int. J. Extrem. Manuf.* **2023**, *5*, 32001.
29. Pobel CR, Arnold C, Osmanlic F, Fu Z, Körner C. Immediate development of processing windows for selective electron beam melting using layerwise monitoring via backscattered electron detection. *Mater. Lett.* **2019**, *249*, 70–72.
30. Normenausschuss Materialprüfung (NMP). *Prüfung Metallischer Werkstoffe—Zugproben 77.040.10, 50125*; Beuth Verlag GmbH: Berlin, Germany, 2016.
31. Normenausschuss Materialprüfung (NMP). *Prüfung Von Metallischen Werkstoffen—Druckversuch an Metallischen Zellularen Werkstoffen 77.040.10, 50134*; Beuth Verlag GmbH: Berlin, Germany, 2008.
32. Fu J, Hu Z, Song X, Zhai W, Long Y, Li H, et al. Micro selective laser melting of NiTi shape memory alloy: Defects, microstructures and thermal/mechanical properties. *Opt. Laser Technol.* **2020**, *131*, 106374.
33. Breuning C, Arnold C, Markl M, Körner C. A multivariate meltpool stability criterion for fabrication of complex geometries in electron beam powder bed fusion. *Addit. Manuf.* **2021**, *45*, 102051.
34. Abas RA, Hayashi M, Seetharaman S. Thermal Diffusivity Measurements of CMSX-4 Alloy by the Laser-Flash Method. *Int. J. Thermophys.* **2007**, *28*, 109–122.
35. Faulkner MG, Amalraj JJ, Bhattacharyya A. Experimental determination of thermal and electrical properties of Ni-Ti shape memory. *Smart Mater. Struct.* **2000**, *5*, 632–639.
36. Tan C, Li S, Essa K, Jamshidi P, Zhou K, Ma W, et al. Laser Powder Bed Fusion of Ti-rich TiNi lattice structures: Process optimisation, geometrical integrity, and phase transformations. *Int. J. Mach. Tools Manuf.* **2019**, *141*, 19–29.
37. Ono N, Satoh A, Ohta H. A Discussion on the Mechanical Properties of Shape Memory Alloys Based on a Polycrystal Model. *Mater. Trans. JIM* **1989**, *30*, 756–764.
38. Mecking H, Kocks UF, Hartig C. Taylor factors in materials with many deformation modes. *Scr. Mater.* **1996**, *35*, 465–471.
39. Laplanche G, Birk T, Schneider S, Frenzel J, Eggeler G. Effect of temperature and texture on the reorientation of martensite variants in NiTi shape memory alloys. *Acta Mater.* **2017**, *127*, 143–152.
40. Otsuka K, Ren X. Physical metallurgy of Ti–Ni-based shape memory alloys. *Prog. Mater. Sci.* **2005**, *50*, 511–678.
41. Sridhar SK, Stebner AP, Rollett AD. Statistical variations in predicted martensite variant volume fractions in superelastically deformed NiTi modeled using habit plane variants versus correspondence variants. *Int. J. Solids and Struct.* **2021**, *221*, 60–76.
42. Gall K. The role of texture in tension–compression asymmetry in polycrystalline NiTi. *Int. J. Plast.* **1999**, *15*, 69–92.
43. Zhu YT, Liao XZ, Wu XL, Narayan J. Grain size effect on deformation twinning and detwinning. *J. Mater. Sci.* **2013**, *48*, 4467–4475.
44. Ishida Y, Brown M. Dislocations in grain boundaries and grain boundary sliding. *Acta Metall.* **1967**, *15*, 857–860.
45. Bartlett JL, Li X. An overview of residual stresses in metal powder bed fusion. *Addit. Manuf.* **2019**, *27*, 131–149.
46. Denlinger ER, Gouge M, Irwin J, Michaleris P. Thermomechanical model development and in situ experimental validation of the Laser Powder-Bed Fusion process. *Addit. Manuf.* **2017**, *16*, 73–80.
47. Sehitoglu H, Wu Y, Alkan S, Ertekin E. Plastic deformation of B2-NiTi—Is it slip or twinning? *Philos. Mag. Lett.* **2017**, *97*, 217–228.